

# In Situ Identification and Time-Resolved Observation of the Interfacial State and Reactive Intermediates on a Cobalt Oxide Nanocatalyst for the Oxygen Evolution Reaction

Yangming Lin,\* Linhui Yu, Ling Tang, Feihong Song, Robert Schlögl, and Saskia Heumann\*



Cite This: *ACS Catal.* 2022, 12, 5345–5355



Read Online

ACCESS |



Metrics & More



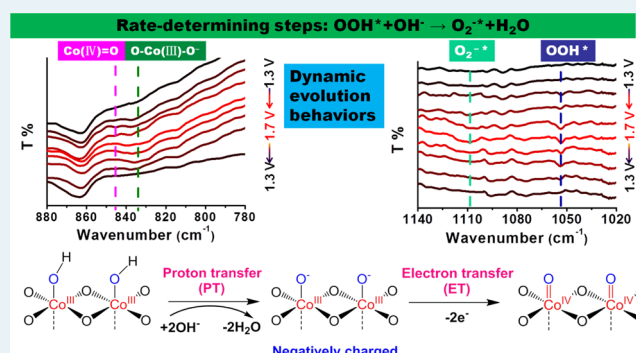
Article Recommendations



Supporting Information

**ABSTRACT:** Cobalt oxide (assigned as  $\text{CoO}_x$ ) is an efficient oxygen evolution reaction (OER) nanocatalyst, which has been extensively studied as a replacement to noble metal-based catalysts. The recent observations and understandings for the interfacial state, adsorbed intermediate products, and rate-determining steps (RDS) on  $\text{CoO}_x$  however, have remained elusive because of the dynamic transformation of different Co ions and the transient nature of the intermediates formed during the OER process. In this work, we propose that under the chosen experimental conditions, the redox process between Co(III) and Co(IV) species does not follow a proton-coupled electron transfer mechanism that is thought to be common prior to the OER, but it involves a proton-decoupled electron transfer, clarified by isotope labeling experiments and *in situ* electrostatic modulation. The interfacial state of  $\text{CoO}_x$  is negatively charged prior to the formation of Co(IV)=O species. The theoretical concentration of the resulting Co(IV)=O species is approximately  $0.1229 \times 10^{19} \text{ cm}^{-2}$ . The Co(IV)=O species are demonstrated to directly regulate the OER performance. Moreover, we experimentally monitor the dynamic evolution behaviors of Co(IV)=O,  $\text{Co(O)O}^-$ ,  $\text{OOH}^*$ , and  $\text{O}_2^{-*}$  intermediates during the OER with *in situ* time-resolved infrared spectroscopy, and the following elementary step  $\text{OOH}^* + \text{OH}^- \rightarrow \text{OO}^{-*} + \text{H}_2\text{O}$  is likely to be the unexpected RDS in the OER process.

**KEYWORDS:** time-resolved spectroscopy, oxygen evolution reaction, water splitting, dynamic behavior, active sites, isotope labeling



## INTRODUCTION

The oxygen evolution reaction (OER) is one of the most important technological reactions for renewable energy storage systems such as water electrolyzers, fuel cells, and metal–air batteries.<sup>1–3</sup> When driven with voltage, the OER is a thermodynamic downhill reaction involving the distribution of multiple oxidation processes over a narrow potential range and the coupling of multiple proton and electron transfers.<sup>4</sup> Conductive first-row transition metal oxides as potential catalysts have been shown to promote the OER with a low cost, sustainability, and high efficiency.<sup>5</sup> Among these oxides, cobalt oxide (assigned as  $\text{CoO}_x$ ) is one of the most representative binary nanocatalysts. The electrocatalytic activity of  $\text{CoO}_x$  is mainly dominated by its surface area, exposed crystal facets, surface oxygen vacancies, and electronic states. Recently, different Co ions including Co(II), Co(III), and Co(IV) have been proposed to be active sites with various investigation methods.<sup>6–11</sup> The surface/interfacial states of  $\text{CoO}_x$  are subject to the formation of Co–oxo species, such as cobalt oxyhydroxide ( $\text{CoOOH}$ ) and  $\text{CoO}_2$  intermediates, prior to or during the OER, which also act as potential active phases.<sup>12,13</sup> For example, Mefford et al. reported that  $\beta$ -

$\text{Co(OH)}_2$  was found to be inactive for the OER, while  $\beta$ - $\text{CoOOH}$  and  $\text{CoO}_2$  were suggested to be potentially active phases for the OER.<sup>14</sup> Density functional theory (DFT) calculations have been used generally to reveal some possible elementary steps (most of them contain 4–5 steps) based on the proton-coupled electron transfer (PCET) mechanism during the OER process.<sup>15</sup> The possible rate-determining step (RDS) was admitted to the formation of key intermediate O–O bonds with DFT calculations and Tafel slopes, and the adsorbate evolving mechanism was widely used to explain the formation of  $\text{O}_2$ .<sup>16,17</sup> Interestingly, combined with thermodynamic and steady-state microkinetic approaches, different RDS and involved mechanism theories have been proposed for  $\text{CoO}_x$ . Taking  $\text{CoO}_2$  intermediate originating from the

Received: December 6, 2021

Revised: March 3, 2022

Published: April 19, 2022



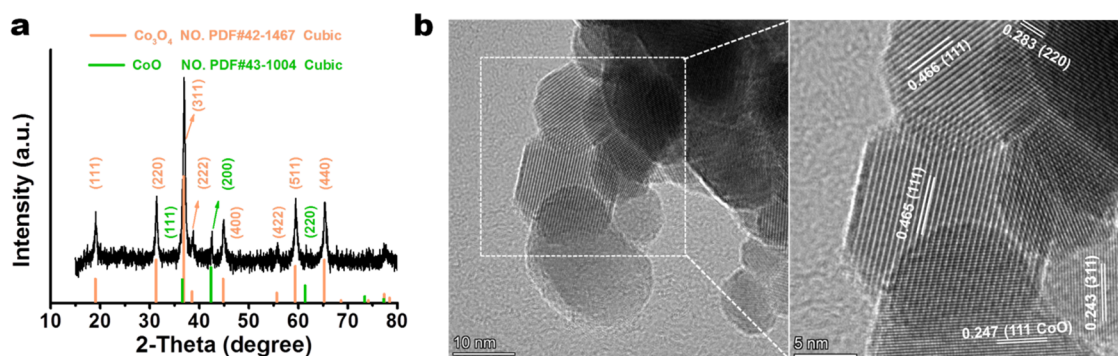


**Figure 1.** Physical characterizations of  $\text{CoO}_x$ . (a) XRD. (b) HRTEM at different resolutions. The scale bars are 10 and 5 nm.

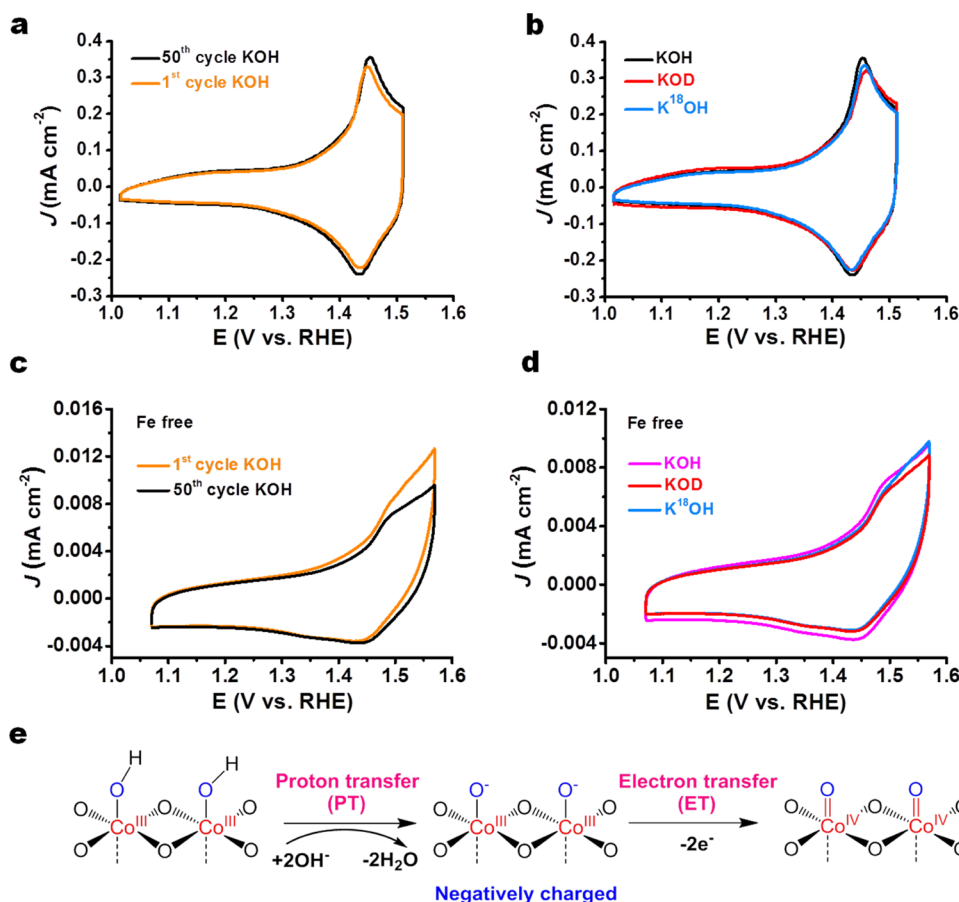


**Figure 2.** Electrochemical measurements of  $\text{CoO}_x$  in different media. (a) Cyclic voltammogram (CV) curves of  $\text{CoO}_x$  at  $50 \text{ mV s}^{-1}$  scan rate for 50 scans in 0.1 M standard KOH. (b) fiftieth CV curves of  $\text{CoO}_x$  measured with isotope-labeled electrolytes with  $iR$  correction. The concentration of the electrolytes is 0.1 standard M. (c, d) CV curves of  $\text{CoO}_x$  in 0.1 M purified electrolytes. (e) Possible oxidation process of Co(III) to Co(IV) involving a proton transfer (PT)-decoupled electron transfer (ET) mechanism. Here, two octahedral structures bridged with O atoms were used as an ideal model because Co(III) typically lies in the octahedral site. Using two octahedral structures was only applied to roughly describe the possible interfacial state of  $\text{CoO}_x$ .

oxidation of  $\text{CoO}_x$  during the OER as an example, its potential limiting step was found to be the deprotonation process of the adsorbed OH species (that is  $\text{OH}^* \rightarrow \text{O}^*$ ), while the RDS was determined to be the adsorption process of  $-\text{OH}$  on active sites (that is  $* \rightarrow \text{OH}^*$ ).<sup>14</sup> Additionally,  $\text{O}_2$  generated on some highly active oxides can come from lattice O instead of the conventional  $-\text{OH}$  adsorbate evolving mechanism clarified by *in situ* mass spectrometry.<sup>18</sup> Therefore, the mechanistic understanding of the OER at  $\text{CoO}_x$  is a matter of controversy, and it is still not well-understood partially because of the

dynamic transformation of different Co–oxo species and the transient nature of the formed intermediate oxygen species upon oxidation potential. In short, elucidation of the key mechanism and intermediates of the conversion of  $\text{H}_2\text{O}$  to  $\text{O}_2$  on a  $\text{CoO}_x$  surface may provide valuable insights into oxygen-evolving solid oxide catalysts in general.

Combination of spectroelectrochemical characterization techniques and isotope labeling experiments allows us to study *in situ* the reaction process at the electrode interface without affecting the performance of the catalyst and can

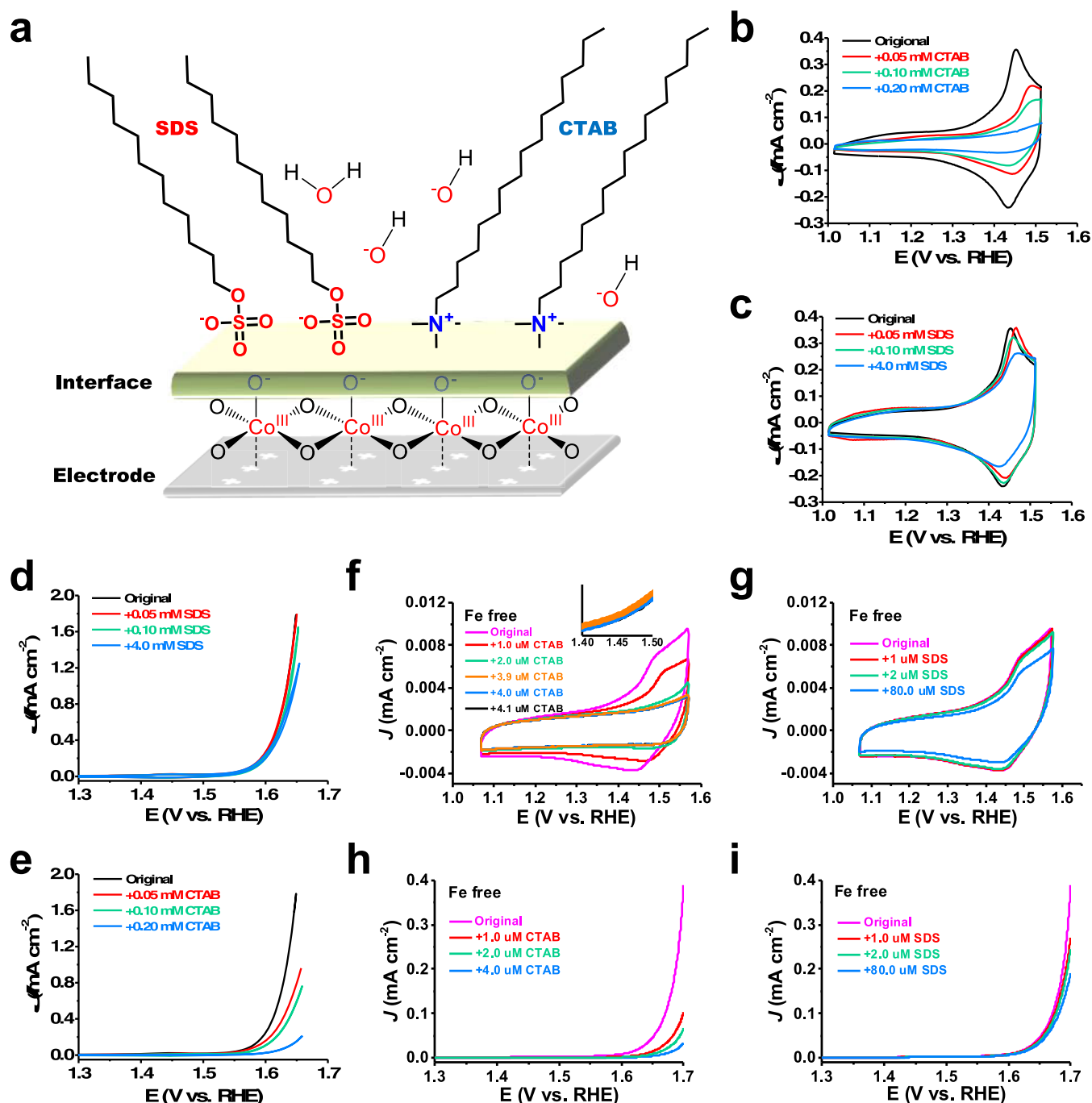


**Figure 3.** *In situ* electrostatic adsorption for interfacial state identification on CoO<sub>x</sub> at potentials above 1.3 V<sub>RHE</sub> in standard KOH and purified KOH. (a) Schematic Illustration of the electrostatic interaction between the interface of CoO<sub>x</sub> terminated with the oxygen anion and the cationic surfactant (CTAB)/anionic surfactant (SDS). Here, four octahedral structures bridged with O atoms were used as an ideal model. (b, c) CV curves of Co species in the presence of CTAB/SDS at different concentrations, respectively, to investigate the relationships between the redox peaks. (d, e) LSV curves of CoO<sub>x</sub> in the presence of CTAB/SDS with different concentrations, respectively. (f–i) CV and LSV curves of CoO<sub>x</sub> using purified KOH as an electrolyte in the presence of CTAB/SDS at different concentrations, respectively. The inset of f is the partially enlarged region at the specific potential window of 1.4–1.5 V on CTAB with 3.9 μM (orange line), 4.0 μM (sky blue line), and 4.1 μM (black line) contents. All data are corrected by *iR*.

therefore be used to track the changes in the CoO<sub>x</sub> during the OER. Under the chosen experimental conditions, we propose an unexpected evolution process of Co(III) to Co(IV) species. Different from the reported PCET mechanism, a proton transfer (PT)-decoupled electron transfer (ET) is involved. Our results indicate that the interfacial state of CoO<sub>x</sub> is negatively charged and is terminated by oxygen anion species

prior to the formation of Co(IV) species. We also demonstrate a positive relationship between the concentration of Co(IV) species and the OER performance with *in situ* electrostatic adsorption. Specifically, key peroxide OOH\* and O<sub>2</sub><sup>-\*</sup> intermediates are monitored during the OER. Together with the kinetic isotope effect (KIE), a possible RDS involving a

deprotonation process rather than conventional O–O bond formation is shown experimentally.

## RESULTS AND DISCUSSION

***In Situ* Identification of the Oxidation Process of Co(III) to Co(IV) and the Interfacial State and Quantification of the Active Phase.** Recently, extensive research has been conducted to explore the reactive roles of different Co species in the OER. In general, due to the presence of structural defects, such as oxygen vacancies, some Co species will be possibly exposed in the form of cations. Such Co cations enable first the absorption of OH<sup>−</sup> species and then the formation of active Co species with higher oxidation states, which are terminated with oxygen species at a specific oxidative potential. The most common PCET mechanism has been proposed for the formation of Co(IV)=O species on CoO<sub>x</sub>, in which the terminated –OH groups will donate one proton simultaneously combined with one electron to complete the oxidation of Co(III)–OH to Co(IV)=O species.<sup>19</sup> However, such a concerted PCET mechanism may not be considered as an elementary reaction and does not provide evidence about the detailed interfacial state of CoO<sub>x</sub> during the oxidation process.

In the present work, we used commercial CoO<sub>x</sub> as a model that was basically characterized. As displayed in Figure 1a, CoO<sub>x</sub> consists of Co<sub>3</sub>O<sub>4</sub> and CoO, and its crystal phase mainly involves cubic structures as indicated by X-ray powder diffraction (XRD) characteristic peaks of different facets. High-resolution transmission electron microscopy (HRTEM) images were applied to observe the morphology of the catalyst (Figure 1b). The particle size of CoO<sub>x</sub> is in the nanoscale region. The identified interlayer spacings of 0.283, 0.243, and 0.465 nm correspond to (220), (311), and (111) of Co<sub>3</sub>O<sub>4</sub>, respectively. Additionally, (111) of CoO is found based on its interlayer spacings of 0.247 nm. The results of HRTEM are consistent with the XRD results. With the four-point probe method, the conductivity of the used CoO<sub>x</sub> was determined to be about  $3 \times 10^{-4}$  S cm<sup>−1</sup>.

Figure 2a shows an anodic peak of the CoO<sub>x</sub> sample in the cyclic voltammogram (CV) at around 1.45 V vs RHE ( $V_{\text{RHE}}$ ), which is assigned to the transformation of Co(III)–oxo (typically, Co(III)(O)OH) to Co(IV)–oxo species.<sup>7,11,20,21</sup> After 50 cycles, a slight increase of the intensity is observed. To elucidate the underlying oxidation process on CoO<sub>x</sub> during the formation of Co(IV)=O species, some isotope labeling experiments were carried out (Figure 2b). The substitutions of H with D and <sup>16</sup>O with <sup>18</sup>O have been implemented extensively due to the large differences in reaction rates originating from the reduced mass differences between the isotopes.<sup>22</sup> Ideally, when KOD or K<sup>18</sup>OH is used as a substitute for KOH, the redox wave involving Co(III)–OH to Co(IV)=O species can be expected to be shifted to more positive potentials as a stronger D-bonding relative to the H-bonding network, or a stronger <sup>18</sup>O–H relative to the <sup>16</sup>O–H network can be produced.<sup>23</sup> Here, the position of the redox wave measured with KOD does not obviously shift ( $\Delta = 4$  mV) compared with KOH. Additionally, we do not observe visible peak shifts and current density changes in the case of K<sup>18</sup>OH. These findings suggest that Co(III) cations may not be terminated with –OH species to generate active Co(III)–OH components prior to the appearance of the oxidation peak. Moreover, comparing CV curves operated in KOH, both KOD and K<sup>18</sup>OH do not show any obvious difference in the

separation between oxidation and reduction peaks, reflecting that a proton-involving transfer (PT, PCET) is dominant for the oxidation of Co(III) to Co(IV) species. To study the potential role of the Fe impurity in electrolytes for the redox process, purified electrolytes are obtained, based on the reported treatment method.<sup>24</sup> As shown in Figure 2c, the intensities of the CV peaks obtained in purified KOH are significantly lower than those measured in standard KOH, and their positions shift to more positive potentials ( $\Delta = 35$  mV). After 50 cycles, a decrease of the intensity in CV is observed as the presence of Fe could improve the stability of Co-based catalysts. Of note, compared with standard electrolytes, the redox wave shows similar features in different purified electrolytes (Figure 2d). For example, the position of the redox wave measured with purified KOD and K<sup>18</sup>OH does not obviously shift compared with purified KOH. Based on these results, we propose a possible mechanism concerning the transformation of Co(III) to Co(IV) species, in which a PT-decoupled ET mechanism is suggested (Figure 2e), and ET dominates the oxidation process. The related evidence will be further provided in the following part.

To confirm the interfacial state of CoO<sub>x</sub>, an electrostatic adsorption strategy was used with surfactants, as shown in Figure 3a. Given the surface charge property, cetyltrimethyl ammonium bromide (CTAB) as the most common and stable cationic surfactant was first applied. As a comparison, sodium dodecyl sulfate (SDS) was selected as an anionic surfactant.<sup>25</sup> The contents of CTAB and SDS were controlled below the critical micelle concentration (CMC) to avoid the formation of micelles that could directly cover the electrodes and might change the ionic mobility of the electrolyte.<sup>26</sup> During the collection of CV curves, CTAB and SDS were added *in situ*. After the introduction of CTAB at different concentrations (Figure 3b), the intensity of the redox peaks gradually decreases, suggesting that less and less Co(III)–OH species will be oxidized to Co(IV)=O species. Moreover, the redox peaks profoundly shift to higher potentials ( $\Delta = 40$  mV for the oxidation peak and  $\Delta = 20$  mV for the reduction peak), indicating that there is a strong electrostatic interaction occurring between the interface of CoO<sub>x</sub> and the CTAB. Attenuated total reflectance infrared (ATR-IR) spectra support this fact based on the shift of C–N vibration on CTAB and CTAB + CoO<sub>x</sub> samples (Figure S1a). It should be noted that the incorporation of SDS does not obviously influence the intensity and the position ( $\Delta = 6$  mV) of redox peaks, even using 4.0 mM SDS (Figure 3c). Furthermore, no shift of the S=O vibrations could be determined for the SDS + CoO<sub>x</sub> sample in comparison to the pure SDS in the ATR-IR spectra (Figure S1b). This reflects that no electrostatic interaction takes place between the interface of CoO<sub>x</sub> and the SDS. Moreover, *in situ* electrostatic adsorption experiments were carried out in purified KOH to exclude the influence of the Fe impurity. As shown in Figure 3f,g, CV and LSV results collected from purified KOH show similar features in comparison to standard KOH, suggesting a noncritical role of Fe in the interfacial state of CoO<sub>x</sub> except for current density. Combining these results allows us to conclude that (i) the interfacial state of CoO<sub>x</sub> is negatively charged in the form of Co(III)–O<sup>−</sup> species possibly originating from deprotonation of Co(III)–OH species. The form of suggested Co(III)–O<sup>−</sup> species can also be supported by the results of CV curves (Figure 2). Subsequently, the Co(III)–O<sup>−</sup> species donate one electron to form Co(IV)=O species at the elevated potential

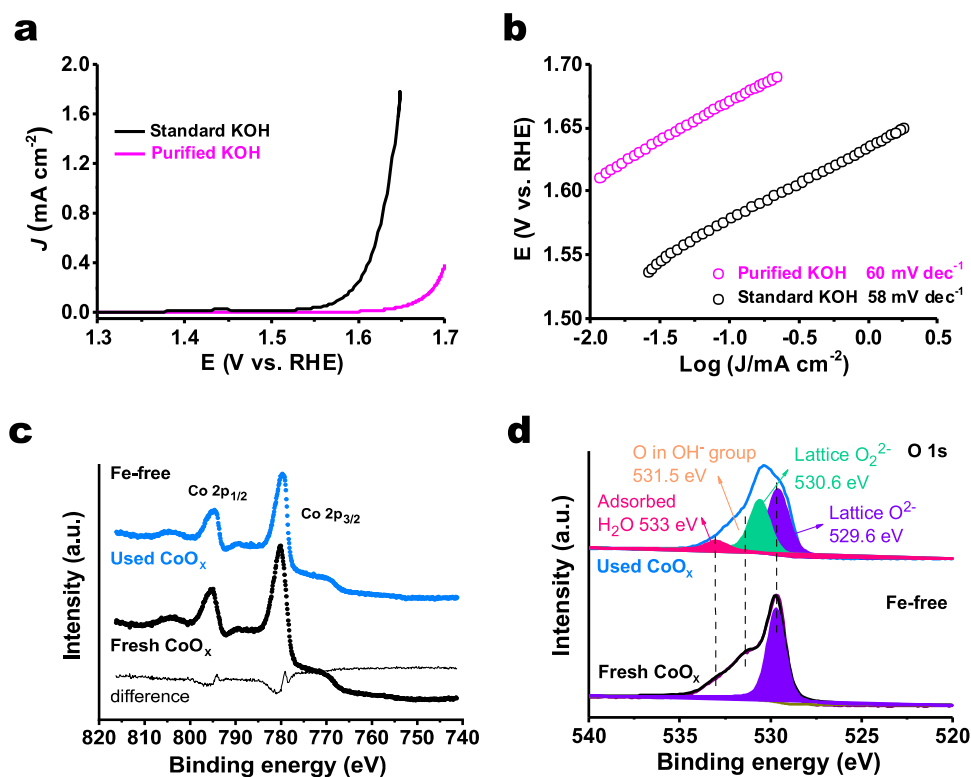


**Figure 4.** (a) LSV curves and (b) Tafel slopes of  $\text{CoO}_x$  measured in standard KOH and purified KOH. The Tafel slopes are calculated at 1.58–1.62 and 1.62–1.69  $V_{\text{RHE}}$  in standard KOH and purified KOH, respectively. XPS spectra of (c, d) fresh  $\text{CoO}_x$  and used  $\text{CoO}_x$  subjected to 30 min potentiostatic electrolysis at 1.65  $V_{\text{RHE}}$  in purified KOH.

(Figure 2e) and (ii) the presence of CTAB could interact with terminal oxygen anion species, ultimately leading to the reduction of the amounts of  $\text{Co(IV)=O}$  species. Previously, the interfacial states of NiFe LDH and  $\text{CoOOH}$  catalysts were proposed to be negatively charged, which was revealed by titration of organic cations and operando Raman spectroscopy, respectively. The former suggested that a negatively charged interface can be attributed to active oxygen species formed upon deprotonation. The latter found that during the OER process, the formation of  $\text{CoOO}^-$  species is responsible for the negatively charged interface.<sup>27,28</sup>

The quantification of surface concentration of  $\text{Co(IV)=O}$  species is of significance to understand the following OER process. In the present work, to have a more accurate access to the theoretical values of  $\text{Co(IV)=O}$  species, we further optimized the concentration of CTAB in purified KOH. As displayed in Figure 3f, the presence of 3.9  $\mu\text{M}$  CTAB shows a little bit higher current density than 4.0  $\mu\text{M}$ , while there is no difference between the concentrations of 4.0 and 4.1  $\mu\text{M}$  on current density. This indicates that at a concentration of 4.0  $\mu\text{M}$  CTAB, saturation for the neutralization of negatively charged interfaces may have been reached. These findings indicate that using *in situ* titration of surfactants to quantify charged Co species is reasonable. By *in situ* addition of CTAB, the  $\text{Co(IV)=O}$  species can be determined to a theoretical value of  $0.1229 \times 10^{19} \text{ cm}^{-2}$  in purified KOH, where we assume that all  $\text{Co(III)-O}^-$  species take part in the formation of  $\text{Co(IV)=O}$  species, and every  $\text{Co(III)-O}^-$  species absorb only one CTAB molecule. Depending on the chemical formulas of  $\text{CoO}_x$ , the percentage of  $\text{Co(III)-O}^-$  species theoretically present on the surface of  $\text{CoO}_x$  is calculated to be 0.06–0.192% in purified KOH.

After sweeping to the OER working potential, a noticeable difference on the current density in the presence of CTAB or SDS could be detected. With increasing concentration of CTAB, the OER performance is gradually reduced, while the onset potential remains constant (Figure 3d). It should be noted that there are no obvious differences in the Faradaic efficiency ( $\text{FE}(\text{O}_2)$ , ~96–98%) and the selectivity of peroxide ( $\text{H}_2\text{O}_2$ , ~0%) in the absence/presence of CTAB (Figure S2a,b). These findings suggest a decreasing amount of active component. This behavior can be explained by less oxidation of  $\text{Co(III)-O}^-$  to  $\text{Co(IV)=O}$  species caused by the electrostatic interaction between  $\text{Co(III)-O}^-$  species and the CTAB. However, the OER performance, the  $\text{FE}(\text{O}_2)$  (95.7%), and the selectivity of  $\text{H}_2\text{O}_2$  (~0%) are independent of the content of SDS (Figures 3e and S2a,c). By calculating the related Tafel slopes (Figure S3a,b) in the absence/presence of CTAB, two facts are reflected: (a) the kinetic reaction rate is not influenced by CTAB and (b) CTAB could interact with its terminal oxygen anion species in an oriented manner rather than roughly covering the whole surface of  $\text{CoO}_x$ . The trends observed in activity and Tafel slopes obtained in CTAB and SDS under Fe-free conditions are analogous to standard KOH (Figures 3h,i and S3c,d). In view of these results, we conclude that under the chosen experimental conditions, (i)  $\text{Co(IV)=O}$  is advantageous to accelerate the OER and (ii) the  $\text{Co(IV)=O}$  concentration can be simply tuned by changing the CTAB concentration.

Furthermore, we compared the activity measured in standard KOH and purified KOH. The result of Figure 4a implies that the absence of Fe significantly decreases the current density of the OER. As reported, the tafel slope will be affected with varying the concentration of Fe in the

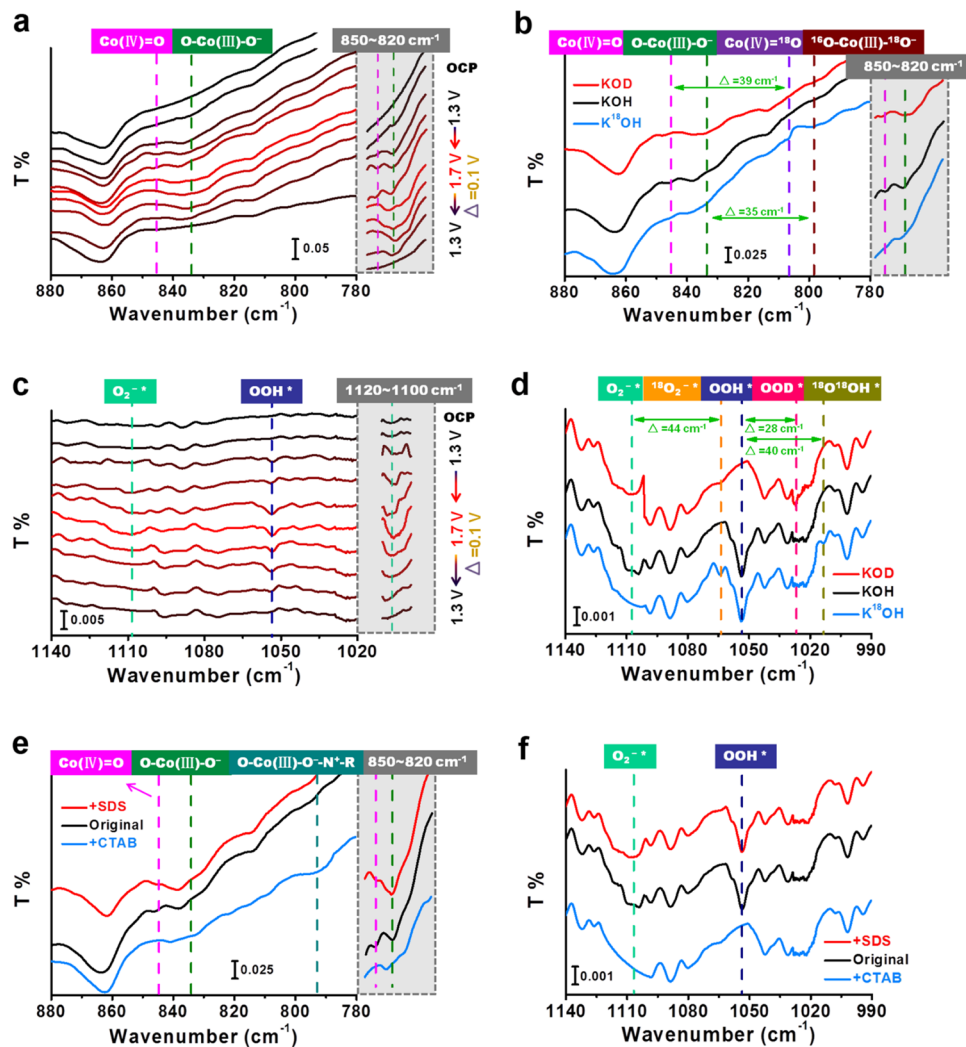


**Figure 5.** *In situ* ATR-IR spectra monitoring and identification of the involved intermediate products during the OER process. (a, b) Active Co-oxo species and (c, d) oxygen species. Here, two specific regions at 820–850 and 1100–1120 cm<sup>-1</sup> are additionally enlarged in (a–c), respectively. Some control experiments including Ar-saturated 0.1 M standard electrolytes (e.g., KOH, KOD, and K<sup>18</sup>OH) were carried out at 1.6 V<sub>RHE</sub>. O<sub>2</sub><sup>-\*</sup> and OOH\* represent the adsorbed O<sub>2</sub><sup>-</sup> and OOH species, respectively. (e, f) Relationships between the intermediate Co-oxo, O<sub>2</sub><sup>-\*</sup>, and OOH\* species and the CTAB/SDS surfactants operated at 1.6 V<sub>RHE</sub>, respectively. N<sup>+</sup>-R stands for the N-containing cationic group of CTAB. All the data were collected after 30 s of potential operation.

electrolyte.<sup>27</sup> The Tafel slope of the Co-based catalyst in purified KOH is about 60 mV dec<sup>-1</sup>. This value will be gradually decreased to about 30–40 mV dec<sup>-1</sup> along with the increase of concentration of Fe. In other words, the incorporation of Fe changes the Co-based intrinsic mechanism of the OER. However, in our present work, the Tafel slope obtained in standard KOH is 60 mV dec<sup>-1</sup> (Figure 4b), while this value does not show marked change in purified KOH (58 mV dec<sup>-1</sup>). Combined with the results of isotope labeling (Figure 2) and *in situ* electrostatic adsorption experiments (Figure 3), it is assumed that the presence or absence of Fe does not have an obvious impact on the OER reaction steps. The chemical compositions of fresh CoO<sub>x</sub> were additionally analyzed by X-ray photoelectron spectra (XPS) (Figure 4c,d). Due to spin–orbit splitting, the Co 2p spectrum consists of two main peaks attributed to Co 2p<sub>1/2</sub> and Co 2p<sub>3/2</sub>. The binding energy of the Co 2p<sub>3/2</sub> peak is about 780.2 eV. Due to similar binding energies between Co(II) and Co(III) compounds,<sup>28,29</sup> the spectrum cannot be used to assign the oxidation state of Co. The O 1s XPS spectrum is divided into

three main peaks: a peak at 529.6 eV related to lattice oxygen (O<sup>2-</sup>), a peak at 531.5 eV assigned to O atoms of surface hydroxyl groups (OH<sup>-</sup>), and one peak at 533 eV associated to the adsorbed water molecules.<sup>29,30</sup> The chemical composition of used CoO<sub>x</sub> after a short-term potentiostatic electrolysis (at 1.65 V<sub>RHE</sub> for 30 min) is depicted, and its Co 2p spectrum shows only minor differences compared to fresh CoO<sub>x</sub>. A new peak appeared at about 530.6 eV in the O 1s spectrum, which was previously attributed to peroxo-like species (O<sub>2</sub><sup>2-</sup>).<sup>31,32</sup>

***In Situ* Time-Resolved Observation of Reactive Intermediates and Determination of the Rate-Determining Step.** With density functional theory calculations, Co-oxo intermediate species have been predicted as commonly active platforms to proceed the absorption/desorption of surface intermediate oxygen species (e.g., OH\*, O\*, and OOH\*) that mainly dominate the OER process.<sup>33,34</sup> Some achievements have been conducted to experimentally determine Co-oxo species and their valence states with *ex situ* electron paramagnetic resonance and X-ray absorption near-edge structure spectroscopy.<sup>11,35</sup> For other metal oxides, such

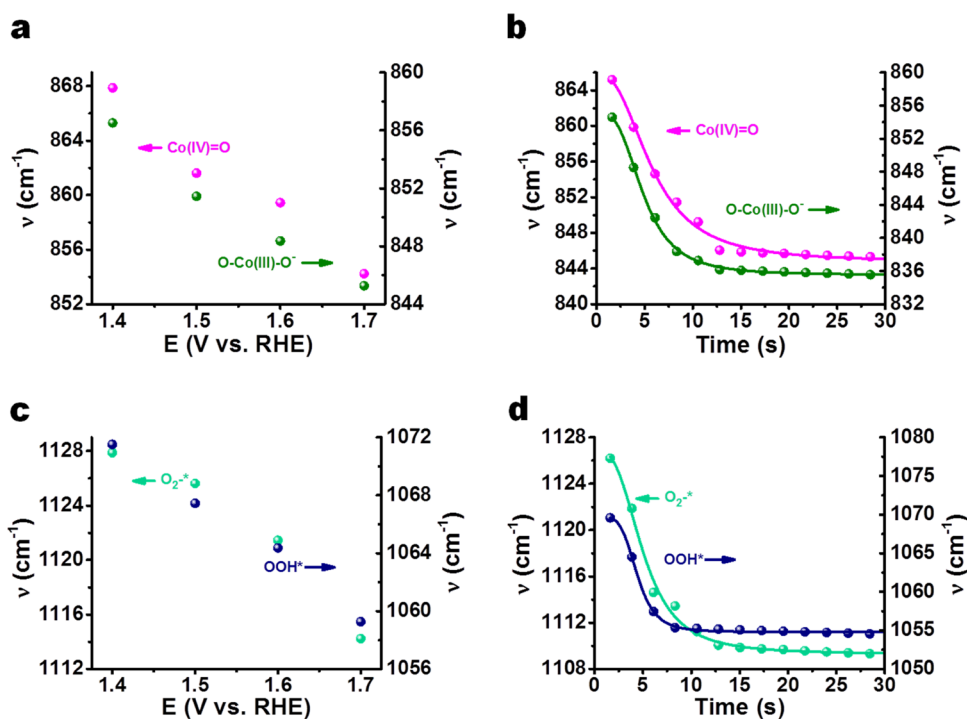


**Figure 6.** IR band analysis of time-resolved ATR spectra. (a)  $\nu_{\text{Co(IV)=O}}$  and  $\nu_{\text{O-Co(III)-O}^-}$  observed in the first 4 s during chronoamperometric scan from 1.4 to 1.7 V and (b) during a real-time scan (with fitting lines) at 1.6 V for 30 s in a standard KOH electrolyte. (c)  $\nu_{\text{OOH}^*}$  and  $\nu_{\text{O}_2^*}$  observed in the first 4 s during chronoamperometric scan from 1.4 to 1.7 V and (d) during real-time scan (with fitting lines) at 1.6 V for 30 s in a standard KOH electrolyte.

as  $\text{Fe}_2\text{O}_3$  and  $\text{TiO}_2$ , transient absorption spectroscopy and *in situ* infrared spectroscopy were used to observe the potential surface peroxide moieties during the photodriven OER process.<sup>36,37</sup> However, the exact role of Co-oxo species, the precise nature of critical mechanistic steps such as O–O bond formation, and the observation of intermediate oxygen species still remain the subject of debate. In the present work, *in situ* attenuated total reflectance infrared (ATR-IR) spectroscopy was applied to elucidate the evolution processes of the surface relevant species and their importance during the OER process. As shown in Figure 5a, the spectrum obtained under open-circuit potential (OCP) conditions does not show difference compared to the spectrum performed at 1.3  $V_{\text{RHE}}$ . The peak located at 845  $\text{cm}^{-1}$  exhibits a reversible behavior with potential change. Interestingly, this peak shows the highest intensity at 1.6  $V_{\text{RHE}}$  rather than at 1.7  $V_{\text{RHE}}$ , suggesting that the formation rate of the corresponding species at 1.7  $V_{\text{RHE}}$  is equal to its subsequent reaction rate triggered by other intermediate species. The peak located at 835  $\text{cm}^{-1}$  exhibits a reversible potential-dependent behavior, and it initially emerges at 1.3  $V_{\text{RHE}}$ , indicating its appearance earlier than that of the species observed at 845  $\text{cm}^{-1}$ . Given that OO stretching modes of Co(III)OOH typically lie in the region of 920–740  $\text{cm}^{-1}$ ,<sup>38</sup> we used an isotope labeling strategy to determine these two species. No obvious change for these two peaks appeared at 835 and 845  $\text{cm}^{-1}$  positions when KOD was used as an electrolyte (Figure 5b), whereas some obvious red shifts could be monitored in  $\text{K}^{18}\text{OH}$  electrolyte. This indicates that these two species contain only oxygen atoms and no protons. Thus, the peak appearing at 835  $\text{cm}^{-1}$  does not belong to Co(III)OOH moieties. As mentioned above, O–Co(III)–OH moieties easily generate O–Co(III)–O<sup>−</sup> moieties by deprotonation prior to 1.3  $V_{\text{RHE}}$ . We therefore propose

that the peak appearing at 835  $\text{cm}^{-1}$  is most likely related to O–Co(III)–O<sup>−</sup> moieties. This finding is analogous to the proposed CoO<sup>−</sup> (~840  $\text{cm}^{-1}$ ) and (O–Ni(III)–O)<sup>−</sup> (~849  $\text{cm}^{-1}$ ) moieties.<sup>39,40</sup> Additionally, the reported frequency shift associated with OO isotope exchange is between 20 and 30  $\text{cm}^{-1}$  for partially labeled ( $^{18}\text{O}^{16}\text{O}$ ) moieties and between 44 and 61  $\text{cm}^{-1}$  for fully labeled ( $^{18}\text{O}^{18}\text{O}$ ) moieties.<sup>38,41</sup> Similar shift results were reported with operando Raman spectroscopy.<sup>28</sup> The appearance of the 835  $\text{cm}^{-1}$  band with an  $^{18}\text{O}$  isotopic shift of 35  $\text{cm}^{-1}$  probably indicates a  $^{16}\text{O}$ –Co(III)– $^{18}\text{O}$  moiety rather than a  $^{18}\text{O}$ –Co(III)– $^{18}\text{O}$  moiety. The observed shift of 39  $\text{cm}^{-1}$  of the  $^{18}\text{O}$  labeled and nonlabeled species agrees well with Co(IV)=O moieties as reported for a CoO<sub>x</sub> surface, which is characterized by hole injection of a visible light sensitizer and an  $\text{S}_2\text{O}_8^{2-}$  electron acceptor.<sup>42</sup> In addition, the onset potential of this absorption peak is 1.4  $V_{\text{RHE}}$  (Figure 5a), at which the oxidation process of Co(III)–O<sup>−</sup> to Co(IV)=O species was occurring. This finding further indicates that the absorption peaks at 845 and 806  $\text{cm}^{-1}$  might be Co(IV)=O and Co(IV)= $^{18}\text{O}$  species, respectively.

Moreover, dynamic evolution processes are monitored by two other peaks located at 1108 and 1054  $\text{cm}^{-1}$  (Figure 5c). Given that the infrared vibration peaks of the O<sub>2</sub><sup>−\*</sup> and OOH<sup>\*</sup> are typically located in the ranges of 1200–1070 and 1100–980  $\text{cm}^{-1}$ ,<sup>43–46</sup> respectively, some control experiments were carefully introduced, to further differentiate O<sub>2</sub><sup>−\*</sup> and OOH<sup>\*</sup> species. The results of Figure 5d reveal that (i) an apparent red-shift behavior ( $\Delta = \sim 28 \text{ cm}^{-1}$ ) appears at the 1026  $\text{cm}^{-1}$  position for KOD electrolyte, whereas the other vibration band at 1108  $\text{cm}^{-1}$  is unaffected, indicating that the vibration band at 1054  $\text{cm}^{-1}$  is most likely to be OOH<sup>\*</sup> rather than O<sub>2</sub><sup>−\*</sup> species; thus, the vibration band at 1108  $\text{cm}^{-1}$  might be

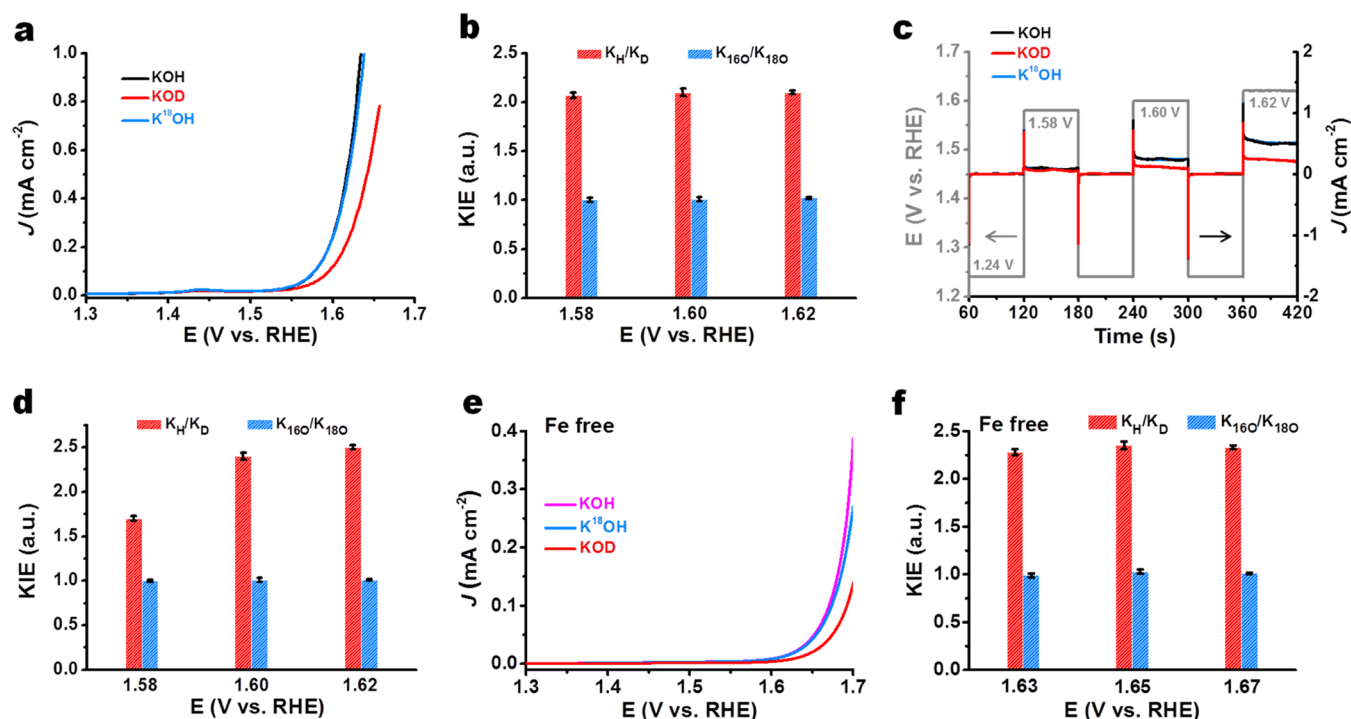


**Figure 7.** Isotope electrochemical studies and determination of possible rate-determining steps of  $\text{CoO}_x$ . (a) LSV curves performed in Ar-saturated 0.1 M standard electrolytes. (b) Kinetic isotope effect (KIE) values measured at different potentials. Here, KIE values are calculated by  $\text{KIE} = k_{\text{H}}/k_{\text{D}} = j_0^{\text{H}}\text{C}_0^{\text{D}}/j_0^{\text{D}}\text{C}_0^{\text{H}}$  or  $\text{KIE} = k_{16\text{O}}/k_{18\text{O}} = j_0^{16\text{O}}\text{C}_0^{18\text{O}}/j_0^{18\text{O}}\text{C}_0^{16\text{O}}$ . (c) Chronoamperometry (CP) protocol (gray) showing an oxidative and reductive bias with the current response in different standard electrolytes. (d) KIE values measured at different potentials. Here, KIE values are calculated by the ratios of steady-state current density at different potentials (at 180, 300, and 420 s, respectively). (e) LSV curves performed in Ar-saturated 0.1 M purified electrolytes. (f) Kinetic isotope effect (KIE) values measured at different potentials with purified electrolytes.

ascribed to  $\text{O}_2^{-*}$ ; (ii) a significant red-shift behavior ( $\Delta = \sim 44 \text{ cm}^{-1}$ ) occurring at the  $1064 \text{ cm}^{-1}$  position can be observed in  $\text{K}^{18}\text{OH}$ , further suggesting that the vibration band at  $1108 \text{ cm}^{-1}$  belongs to  $\text{O}_2^{-*}$  (Figure 5d); and (iii) there is a red-shift behavior ( $\Delta = \sim 40 \text{ cm}^{-1}$ ) existing at the  $1014 \text{ cm}^{-1}$  position in  $\text{K}^{18}\text{OH}$ , which can be assigned to fully labeled  $^{18}\text{O}^{18}\text{OH}$  species. The resulting  $^{18}\text{O}_2^{-*}$  and  $^{18}\text{O}^{18}\text{OH}$  species indicate that  $\text{CoO}_x$  involves a conventional  $-\text{OH}$  adsorbate evolving mechanism. Additionally,  $\text{O}_2^{-*}$  and  $\text{OOH}^*$  species cannot be observed under OCP conditions (Figure 5c).

The relationships between the intermediate Co-oxo and oxygen species and the surfactants are studied. After the introduction of SDS, we do not find any apparent change in  $\text{Co(IV)=O}$ ,  $\text{O-Co(III)-O}^-$ ,  $\text{O}_2^{-*}$ , and  $\text{OOH}^*$  species (Figure 5e,f). It should be noted that after adding CTAB, the  $\text{Co(IV)=O}$  species disappear, and a red shift of partial  $\text{O-Co(III)-O}^-$  species to  $792 \text{ cm}^{-1}$  attributing to the electrostatic interaction between oxygen anion species (i.e.,  $\text{Co(III)-O}^-$ ) and the N-containing cationic group ( $\text{N}^+-\text{R}$ ) of CTAB is monitored. Meanwhile, both  $\text{O}_2^{-*}$  and  $\text{OOH}^*$  species vanish away in the presence of CTAB. It was mentioned above that the potential for the formation/appearance of both  $\text{O}_2^{-*}$  and  $\text{OOH}^*$  species is  $1.4 \text{ V}_{\text{RHE}}$  (Figure 5c), which is consistent with the formation of  $\text{Co(IV)=O}$  (Figure 5a). All these results demonstrate that (i) the onset potential of the OER is around  $1.4 \text{ V}_{\text{RHE}}$  at which  $\text{Co(IV)=O}$  species were partially formed, but the amount is still low; (ii)  $\text{Co(IV)=O}$  species rather than  $\text{Co(III)-oxo}$  species play the critical role in proceeding the OER; and (iii) the formation of  $\text{O}_2^{-*}$  and  $\text{OOH}^*$  species is associated with  $\text{Co(IV)=O}$  sites.

The relationships between IR peak positions and applied potentials are shown in Figure 6a,c. With increasing potentials, IR signals of  $\text{Co(IV)=O}$ ,  $\text{O-Co(III)-O}^-$ ,  $\text{O}_2^{-*}$ , and  $\text{OOH}^*$  exhibit a red-shift behavior. It can be attributed to the Stark effect.<sup>47</sup> All species show similar slopes of the shift ( $d\nu/d\Phi$ , approximately  $40 \text{ cm}^{-1} \text{ V}^{-1}$ ). Further kinetic investigation of these four species during the OER was fulfilled by time-resolved ATR-IR analysis on the time scale of seconds at  $1.6 \text{ V}_{\text{RHE}}$ . As shown in Figure 6b,d,  $\text{Co(IV)=O}$ ,  $\text{O-Co(III)-O}^-$ ,  $\text{OOH}^*$ , and  $\text{O}_2^{-*}$  show similar tendencies, suggesting that they have highly correlated kinetic relationships. At an early stage (10–15 s), the species exhibit an obvious red-shift behavior during real-time scan. It may be attributed to the steric hindrance effect between the Co species ( $\text{Co(IV)=O}$  and  $\text{O-Co(III)-O}^-$ ) and adsorbed  $\text{OOH}^*$  and the generation of the follow-up  $\text{O}_2^{-*}$  species from  $\text{OOH}^*$ . After 15–30 s, an equilibrium of the Co and adsorbed oxygen species ( $\text{O}_2^{-*}$  and  $\text{OOH}^*$ ) seems to be reached, the peak positions remain constant, suggesting that the dipole coupling effects between adsorbed species tend to be stable. In contrast to a similar equilibrium time between  $\text{Co(IV)=O}$  and  $\text{O-Co(III)-O}^-$  species,  $\text{OOH}^*$  shows a shorter equilibrium time ( $\sim 11 \text{ s}$ ) than that of  $\text{O}_2^{-*}$  ( $\sim 15 \text{ s}$ ), suggesting that the formation of  $\text{O}_2^{-*}$  species originating from  $\text{OOH}^*$  possibly determines the OER reaction.

Depending on the thermodynamic steps, calculated by DFT, the most common rate-determining step (RDS) was suggested to involve the formation of key intermediate O–O bonds (commonly  $\text{O}^* + \text{OH}^- \rightarrow \text{OOH}^* + \text{e}^-$ ). The results of DFT calculations are closely associated with the established model structures to some degree; using effectively experimental



measurements to elucidate the most likely RDS during the OER is therefore imperative. The use of KIE is an established experimental technique to study chemical reactions involving PT and oxygen evolving, and its value is an important indicator to determine the RDS.<sup>48–51</sup> First, pH dependence of steady-state electrode potential at a constant current (0.2 mA/cm<sup>2</sup>) in KOH with varying concentrations was studied with the chronoamperometry (CP) protocol. As shown in Figure S4, the tendency is almost unaffected by repeating the titration in the presence of excess inert electrolyte (0.5 M KNO<sub>3</sub>), suggesting that the diffuse double-layer effects originating from the transport of OH ions (or H<sub>2</sub>O molecules) are ruled out.<sup>19</sup> Isotope-based electrochemical studies were then performed (Figure 7a). Compared with KOH, the use of KOD leads to the reduction of current density of CoO<sub>x</sub>, while the introduction of K<sup>18</sup>OH almost exhibits the same activity. All of them show no distinct difference on the tafel slopes at a specific region (Figure S5). By calculating, the KIE values at different potentials in KOH and K<sup>18</sup>OH are approximately 1.0, indicating that there is no significant primary isotope effect. Theoretically, if the cleavage or the formation of the O–O bonds is involved in the RDS, their KIE ratios should be at least larger than 1.0 because the generation of <sup>18</sup>O–<sup>18</sup>O bonds and <sup>16</sup>O–<sup>16</sup>O bonds could obviously influence reaction rates owing to their different mass values. Herein, we can anticipate that the RDS of the OER process does not involve a cleavage or formation of the O–O bonds (O\* + OH<sup>−</sup> → OOH\* + e<sup>−</sup>). It should be pointed out that KIE values around 2.0–2.1 at different potentials in KOH and KOD are obtained (Figure 7b), suggesting a significantly primary isotope effect.<sup>52</sup> To exclude the impact of capacitance on the current density, a CP protocol was used to collect the steady-state current density (Figure 7c). The calculated KIE values are approximately 1.7–2.5 at different potentials (Figures 7d and S6). Similar results of KIE values and tafel slopes are found in purified electrolytes (Figures 7e,f and S7), suggesting that Fe may not positively affect the OER mechanism. These KIE values based on LSV and CP methods reflect that the RDS of the OER process involves a cleavage of the O–H bonds. It indicates that the introduced deuterated water is most likely to influence the formation of active oxygen species \*O from the deprotonation process of \*OD (OD\* + OD<sup>−</sup> → O\* + D<sub>2</sub>O + e<sup>−</sup>) or hinder the deprotonation process of active oxygen species \*OOD (OOD\* + OD<sup>−</sup> → OO<sup>−</sup>\* + D<sub>2</sub>O). Recently, these two deprotonation processes are the most common steps in the OER.<sup>19,52,53</sup> As mentioned above, OOH\* and OO<sup>−</sup>\* species are distinctly detected with *in situ* ATR-IR. Therefore, we conclude that the following elementary step OOH\* + OH<sup>−</sup> → OO<sup>−</sup>\* + H<sub>2</sub>O is likely to be the potential RDS in the OER process.

## CONCLUSIONS

In summary, we have proposed experimental insights into the interfacial state and transient reactive intermediates of the OER on a CoO<sub>x</sub> catalyst with *in situ* electrostatic modulation, time-resolved ATR-IR, and isotope labeling methods. We introduced an unexpected mechanism concerning the transformation of Co(III) to Co(IV) species, in which the interfacial active Co(III)–OH species first deprotonate to generate Co(III)–O<sup>−</sup> species, followed by the formation of Co(IV)=O species combined with one electron. Co(IV)=O species are very important to proceed the OER and can be quantified *in situ*. The dynamic evolution processes of

Co(IV)=O, Co(III)(O)O<sup>−</sup>, O<sub>2</sub><sup>−</sup>\*, and OOH\* intermediates are monitored and are identified during the OER process. These four species show similar kinetic behaviors and take 11–30 s to achieve the dynamic equilibrium. We believe that the deprotonation process of OOH\* is the most likely RDS in the OER process, evidenced by the reversible emergence of O<sub>2</sub><sup>−</sup>\* intermediates and KIE experiments. This work convincingly discloses important intermediate products and reaction mechanisms of CoO<sub>x</sub> during the OER process, thus providing a revelation for investigating other metal-based catalytic reactions.

## ASSOCIATED CONTENT

### Supporting Information

The Supporting Information is available free of charge at <https://pubs.acs.org/doi/10.1021/acscatal.1c05598>.

Full synthesis and additional characterization data (PDF)

## AUTHOR INFORMATION

### Corresponding Authors

**Yangming Lin** – CAS Key Laboratory of Design and Assembly of Functional Nanostructures, Fujian Institute of Research on the Structure of Matter, Chinese Academy of Sciences, Fuzhou, Fujian 350002, P. R. China; Xiamen Key Laboratory of Rare Earth Photoelectric Functional Materials, Xiamen Institute of Rare Earth Materials, Haixi Institute, Chinese Academy of Sciences, Xiamen 361021, China; Max Planck Institute for Chemical Energy Conversion, 45470 Mülheim an der Ruhr, Germany; [orcid.org/0000-0002-3547-9133](https://orcid.org/0000-0002-3547-9133); Email: [xmlinyangming@fjirsm.ac.cn](mailto:xmlinyangming@fjirsm.ac.cn)

**Saskia Heumann** – Max Planck Institute for Chemical Energy Conversion, 45470 Mülheim an der Ruhr, Germany; [orcid.org/0000-0003-3594-6392](https://orcid.org/0000-0003-3594-6392); Email: [saskia.heumann@cec.mpg.de](mailto:saskia.heumann@cec.mpg.de)

### Authors

**Linhui Yu** – Max Planck Institute for Chemical Energy Conversion, 45470 Mülheim an der Ruhr, Germany

**Ling Tang** – CAS Key Laboratory of Design and Assembly of Functional Nanostructures, Fujian Institute of Research on the Structure of Matter, Chinese Academy of Sciences, Fuzhou, Fujian 350002, P. R. China; Xiamen Key Laboratory of Rare Earth Photoelectric Functional Materials, Xiamen Institute of Rare Earth Materials, Haixi Institute, Chinese Academy of Sciences, Xiamen 361021, China

**Feihong Song** – Max Planck Institute for Chemical Energy Conversion, 45470 Mülheim an der Ruhr, Germany

**Robert Schlögl** – Max Planck Institute for Chemical Energy Conversion, 45470 Mülheim an der Ruhr, Germany; Department of Inorganic Chemistry, Fritz Haber Institute of the Max Planck Society, 14195 Berlin, Germany

Complete contact information is available at: <https://pubs.acs.org/10.1021/acscatal.1c05598>

### Funding

Open access funded by Max Planck Society.

### Notes

The authors declare no competing financial interest.

## ACKNOWLEDGMENTS

The authors thank the Max Planck society for funding. The authors are grateful for the financial support from the Hundred Talent Project of the Haixi Institute of the Chinese Academy of Sciences and the Young Talents Training Program of the Shanghai Branch of the Chinese Academy of Sciences (E229PM01).

## REFERENCES

- (1) McCrory, C. C. L.; Jung, S.; Peters, J. C.; Jaramillo, T. F. Benchmarking heterogeneous electrocatalysts for the oxygen evolution reaction. *J. Am. Chem. Soc.* **2013**, *135*, 16977–16987.
- (2) Suen, N.-T.; Hung, S.-F.; Quan, Q.; Zhang, N.; Xu, Y.-J.; Chen, H. M. Electrocatalysis for the oxygen evolution reaction: recent development and future perspectives. *Chem. Soc. Rev.* **2017**, *46*, 337–365.
- (3) Ding, Y.; Klyushin, A.; Huang, X.; Jones, T.; Teschner, D.; Girgsdies, F.; et al. Cobalt-Bridged Ionic Liquid Polymer on a Carbon Nanotube for Enhanced Oxygen Evolution Reaction Activity. *Angew. Chem., Int. Ed.* **2018**, *57*, 3514–3518.
- (4) Fabbri, E.; Haberer, A.; Walter, K.; Kötz, R.; Schmidt, T. J. Developments and perspectives of oxide-based catalysts for the oxygen evolution reaction. *Catal. Sci. Technol.* **2014**, *4*, 3800–3821.
- (5) Burke, M. S.; Enman, L. J.; Batchellor, A. S.; Zou, S.; Boettcher, S. W. Oxygen evolution reaction electrocatalysis on transition metal oxides and (oxy)hydroxides: activity trends and design principles. *Chem. Mater.* **2015**, *27*, 7549–7558.
- (6) Wang, B.; Tang, C.; Wang, H. F.; Chen, X.; Cao, R.; Zhang, Q. A Nanosized CoNi Hydroxide@Hydroxysulfide Core–Shell Heterostructure for Enhanced Oxygen Evolution. *Adv. Mater.* **2019**, *31*, No. 1805658.
- (7) Wang, H. -Y.; Hung, S. -F.; Chen, H. -Y.; Chan, T. -S.; Chen, H. M.; Liu, B. In operando identification of geometrical-site-dependent water oxidation activity of spinel Co<sub>3</sub>O<sub>4</sub>. *J. Am. Chem. Soc.* **2016**, *138*, 36–39.
- (8) Wang, J.; Ge, X.; Liu, Z.; Thia, L.; Yan, Y.; Xiao, W.; Wang, X. Heterogeneous electrocatalyst with molecular cobalt ions serving as the center of active sites. *J. Am. Chem. Soc.* **2017**, *139*, 1878–1884.
- (9) Yeo, B. S.; Bell, A. T. Enhanced activity of gold-supported cobalt oxide for the electrochemical evolution of oxygen. *J. Am. Chem. Soc.* **2011**, *133*, 5587–5593.
- (10) Risch, M.; Ringleb, F.; Kohlhoff, M.; Bogdanoff, P.; Chernev, P.; Zaharieva, I.; Dau, H. Water oxidation by amorphous cobalt-based oxides: in situ tracking of redox transitions and mode of catalysis. *Energy Environ. Sci.* **2015**, *8*, 661–674.
- (11) Mefford, J. T.; Akbashev, A. R.; Kang, M.; Bentley, C. L.; Gent, W. E.; Deng, H. D.; Alsem, D. H.; Yu, Y.-S.; Salmon, N. J.; Shapiro, D. A.; et al. Correlative operando microscopy of oxygen evolution electrocatalysts. *Nature* **2021**, *593*, 67–74.
- (12) Du, J.; Li, C.; Wang, X.; Jones, T. G.; Liang, H.-P. Cobalt oxyhydroxide with highly porous structures as active and stable phase for efficient water oxidation. *Electrochim. Acta* **2019**, *303*, 231–238.
- (13) Kanan, M. W.; Yano, J.; Surendranath, Y.; Dinca, M.; Yachandra, V. K.; Nocera, D. G. Structure and valency of a cobalt-phosphate water oxidation catalyst determined by in situ X-ray spectroscopy. *J. Am. Chem. Soc.* **2010**, *132*, 13692–13701.
- (14) Mefford, J. T.; Zhao, Z.; Bajdich, M.; Chueh, W. C. Interpreting Tafel behavior of consecutive electrochemical reactions through combined thermodynamic and steady state microkinetic approaches. *Energy Environ. Sci.* **2020**, *13*, 622–634.
- (15) Bajdich, M.; García-Mota, M.; Vojvodic, A.; Nørskov, J. K.; Bell, A. T. Theoretical investigation of the activity of cobalt oxides for the electrochemical oxidation of water. *J. Am. Chem. Soc.* **2013**, *135*, 13521–13530.
- (16) Cai, Z.; Bi, Y.; Hu, E.; Liu, W.; Dwarica, N.; Tian, Y.; et al. Single-crystalline ultrathin Co<sub>3</sub>O<sub>4</sub> nanosheets with massive vacancy defects for enhanced electrocatalysis. *Adv. Energy Mater.* **2018**, *8*, No. 1701694.
- (17) Shinagawa, T.; Garcia-Esparza, A. T.; Takanabe, K. Insight on Tafel slopes from a microkinetic analysis of aqueous electrocatalysis for energy conversion. *Sci. Rep.* **2015**, *5*, No. 13801.
- (18) Grimaud, A.; Diaz-Morales, O.; Han, B.; Hong, W. T.; Lee, Y.-L.; Giordano, L.; et al. Activating lattice oxygen redox reactions in metal oxides to catalyze oxygen evolution. *Nat. Chem.* **2017**, *9*, 457.
- (19) Surendranath, Y.; Kanan, M. W.; Nocera, D. G. Mechanistic studies of the oxygen evolution reaction by a cobalt-phosphate catalyst at neutral pH. *J. Am. Chem. Soc.* **2010**, *132*, 16501–16509.
- (20) Palmas, S.; Ferrara, F.; Vacca, A.; Mascia, M.; Polcaro, A. Behavior of cobalt oxide electrodes during oxidative processes in alkaline medium. *Electrochim. Acta* **2007**, *53*, 400–406.
- (21) Zhang, R.; Zhang, Y.-C.; Pan, L.; Shen, G.-Q.; Mahmood, N.; Ma, Y.-H.; et al. Engineering cobalt defects in cobalt oxide for highly efficient electrocatalytic oxygen evolution. *ACS Catal.* **2018**, *8*, 3803–3811.
- (22) Lin, Y.; Wu, K.-H.; Lu, Q.; Gu, Q.; Zhang, L.; Zhang, B.; et al. Electrocatalytic Water Oxidation at Quinone-on-Carbon: A Model System Study. *J. Am. Chem. Soc.* **2018**, *140*, 14717–14724.
- (23) Tse, E. C. M.; Hoang, T. T.; Varnell, J. A.; Gewirth, A. A. Observation of an inverse kinetic isotope effect in oxygen evolution electrochemistry. *ACS Catal.* **2016**, *6*, 5706–5714.
- (24) Spanos, I.; Tesch, M. F.; Yu, M.; Tüysüz, H.; Zhang, J.; Feng, X.; Müllen, K.; Schlögl, R.; Mechler, A. K. Facile Protocol for Alkaline Electrolyte Purification and Its Influence on a Ni–Co Oxide Catalyst for the Oxygen Evolution Reaction. *ACS Catal.* **2019**, *9*, 8165–8170.
- (25) Myers, D. *Surfactant Science and Technology*; Wiley, 2005.
- (26) Rusling, J. F. Controlling electrochemical catalysis with surfactant microstructures. *Acc. Chem. Res.* **1991**, *24*, 75–81.
- (27) Yang, C.; Fontaine, O.; Tarascon, J.-M.; Grimaud, A. Chemical recognition of active oxygen species on the surface of oxygen evolution reaction electrocatalysts. *Angew. Chem.* **2017**, *129*, 8778–8782.
- (28) Moysiadou, A.; Lee, S.; Hsu, C.-S.; Chen, H. M.; Hu, X. Mechanism of Oxygen Evolution Catalyzed by Cobalt Oxyhydroxide: Cobalt Superoxide Species as a Key Intermediate and Dioxygen Release as a Rate-Determining Step. *J. Am. Chem. Soc.* **2020**, *142*, 11901–11914.
- (29) Biesinger, M. C.; Payne, B. P.; Grosvenor, A. P.; Lau, L. W. M.; Gerson, A. R.; Smart, R. StC. Resolving Surface Chemical States in XPS Analysis of First Row Transition Metals, Oxides and Hydroxides: Cr, Mn, Fe, Co and Ni. *Appl. Surf. Sci.* **2011**, *257*, 2717–2730.
- (30) Yang, J.; Liu, H.; Martens, W. N.; Frost, R. L. Synthesis and Characterization of Cobalt Hydroxide, Cobalt Oxyhydroxide, and Cobalt Oxide Nanodiscs. *J. Phys. Chem. C* **2010**, *114*, 111–119.
- (31) Sathiyaraj, M.; Rousse, G.; Ramesha, K.; Laisa, C. P.; Vezin, H.; Sougrati, M. T.; Doublet, M.-L.; Foix, D.; Gonbeau, D.; Walker, W.; Prakash, A. S.; Ben Hassine, M.; Dupont, L.; Tarascon, J.-M. Reversible Anionic Redox Chemistry in High-Capacity Layered-Oxide Electrodes. *Nat. Mater.* **2013**, *12*, 827–835.
- (32) Sathiyaraj, M.; Abakumov, A. M.; Foix, D.; Rousse, G.; Ramesha, K.; Saubanere, M.; Doublet, M. L.; Vezin, H.; Laisa, C. P.; Prakash, A. S.; Gonbeau, D.; Van Tendeloo, G.; Tarascon, J.-M. Origin of Voltage Decay in High-Capacity Layered Oxide Electrodes. *Nat. Mater.* **2015**, *14*, 230–238.
- (33) García-Mota, M.; Bajdich, M.; Viswanathan, V.; Vojvodic, A.; Bell, A. T.; Nørskov, J. K. Importance of correlation in determining electrocatalytic oxygen evolution activity on cobalt oxides. *J. Phys. Chem. C* **2012**, *116*, 21077–21082.
- (34) Mattioli, G.; Giannozzi, P.; Bonapasta, A. A.; Guidoni, L. Reaction Pathways for Oxygen Evolution Promoted by Cobalt Catalyst. *J. Am. Chem. Soc.* **2013**, *135*, 15353–15363.
- (35) McAlpin, J. G.; Surendranath, Y.; Dinca, M.; Stich, T. A.; Stoian, S. A.; Casey, W. H.; et al. EPR Evidence for Co(IV) Species Produced during Water Oxidation at Neutral pH. *J. Am. Chem. Soc.* **2010**, *132*, 6882–6883.
- (36) Nakamura, R.; Nakato, Y. Primary intermediates of oxygen photoevolution reaction on TiO<sub>2</sub> (rutile) particles, revealed by in situ

FTIR absorption and photoluminescence measurements. *J. Am. Chem. Soc.* **2004**, *126*, 1290–1298.

(37) Pendlebury, S. R.; Barroso, M.; Cowan, A. J.; Sivula, K.; Tang, J.; Grätzel, M.; et al. Dynamics of photogenerated holes in nanocrystalline  $\alpha$ -Fe<sub>2</sub>O<sub>3</sub> electrodes for water oxidation probed by transient absorption spectroscopy. *Chem. Commun.* **2011**, *47*, 716–718.

(38) Nakamoto, K. *Infrared and Raman Spectra of Inorganic and Coordination Compounds*; Wiley, 1997; Vols. 1A and 1B.

(39) Uzunova, E. L.; Mikosch, H.; Nikolov, G. S. Electronic structure of oxide, peroxide, and superoxide clusters of the 3d elements: A comparative density functional study. *J. Chem. Phys.* **2008**, *128*, No. 094307.

(40) Citra, A.; Chertihin, G. V.; Andrews, L.; Neurock, M. Reactions of laser-ablated nickel atoms with dioxygen. Infrared spectra and density functional calculations of nickel oxides NiO, ONiO, Ni<sub>2</sub>O<sub>2</sub>, and Ni<sub>2</sub>O<sub>3</sub>, superoxide NiOO, peroxide Ni(O<sub>2</sub>), and higher complexes in solid argon. *J. Phys. Chem. A* **1997**, *101*, 3109–3118.

(41) Zandi, O.; Hamann, T. W. Determination of photoelectrochemical water oxidation intermediates on haematite electrode surfaces using operando infrared spectroscopy. *Nat. Chem.* **2016**, *8*, 778.

(42) Zhang, M.; De Respinis, M.; Frei, H. Time-resolved observations of water oxidation intermediates on a cobalt oxide nanoparticle catalyst. *Nat. Chem.* **2014**, *6*, 362.

(43) Xi, L. F.; Schwanke, C.; Lange, K. M.; Risch, M. In Situ ATR Infrared Study of Cobalt-Borate Water Oxidation Catalysts. *Mater. Sci. Forum* **2020**, *998*, 123–133.

(44) Suzuki, M.; Ishiguro, T.; Kozuka, M.; Nakamoto, K. Resonance Raman spectra, excitation profiles, and infrared spectra of [N,N'-ethylenebis(salicylideneiminato)]cobalt(II) in the solid state. *Inorg. Chem.* **1981**, *20*, 1993–1996.

(45) Cheng, W.; Zhao, X.; Su, H.; Tang, F.; Che, W.; Zhang, H.; Liu, Q. Lattice-strained metal–organic-framework arrays for bifunctional oxygen electrocatalysis. *Nat. Energy* **2019**, *4*, 115–122.

(46) Baranton, S.; Coutanceau, C.; Garnier, E.; Léger, J.-M. How does  $\alpha$ -FePc catalysts dispersed onto high specific surface carbon support work towards oxygen reduction reaction (ORR)? *J. Electroanal. Chem.* **2006**, *590*, 100–110.

(47) Kim, Y.; Park, S.; Shin, S.-J.; Choi, W.; Min, B. K.; Kim, H.; Kim, W.; Hwang, Y. J. Time-resolved observation of C-C coupling intermediates on Cu electrodes for selective electrochemical CO<sub>2</sub> reduction. *Energy Environ. Sci.* **2020**, *13*, 4301–4311.

(48) Lyons, M. E.; Brandon, M. P. A comparative study of the oxygen evolution reaction on oxidised nickel, cobalt and iron electrodes in base. *J. Electroanal. Chem.* **2010**, *641*, 119–130.

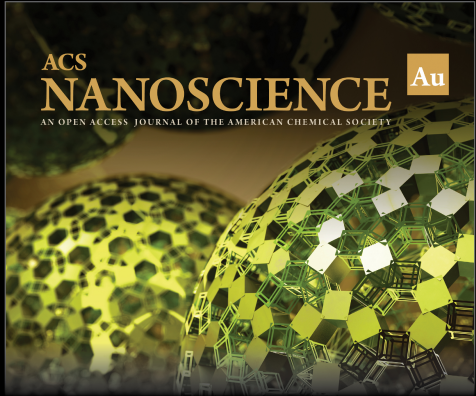
(49) Suntivich, J.; May, K. J.; Gasteiger, H. A.; Goodenough, J. B.; Shao-Horn, Y. A perovskite oxide optimized for oxygen evolution catalysis from molecular orbital principles. *Science* **2011**, *334*, 1383–1385.

(50) Wang, L.-P.; Voorhis, T. V. Direct-coupling O<sub>2</sub> bond forming a pathway in cobalt oxide water oxidation catalysts. *J. Phys. Chem. Lett.* **2011**, *2*, 2200–2204.

(51) Sakaushi, K.; Eckardt, M.; Lyalin, A.; Taketsugu, T.; Behm, R.Jr.; Uosaki, K. Microscopic electrode processes in the four-electron oxygen reduction on highly active carbon-based electrocatalysts. *ACS Catal.* **2018**, *8*, 8162–8176.

(52) Calle-Vallejo, F.; Koper, M. T. First-principles computational electrochemistry: achievements and challenges. *Electrochim. Acta* **2012**, *84*, 3–11.


(53) Trześniewski, B. J.; Diaz-Morales, O.; Vermaas, D. A.; Longo, A.; Bras, W.; Koper, M. T.; Smith, W. A. In situ observation of active oxygen species in Fe-containing Ni-based oxygen evolution catalysts: the effect of pH on electrochemical activity. *J. Am. Chem. Soc.* **2015**, *137*, 15112–15121.




ACS  
**NANOSCIENCE** Au  
AN OPEN ACCESS JOURNAL OF THE AMERICAN CHEMICAL SOCIETY

Editor-in-Chief: **Prof. Shelley D. Minteer**, University of Utah, USA

Deputy Editor:  
**Prof. Raymond E. Schaak**  
The Pennsylvania State University, USA

**Open for Submissions** 

pubs.acs.org/nanoau  ACS Publications  
Most Trusted. Most Cited. Most Read.